PHYSICAL REVIEW APPLIED **13,** 014037 (2020)

Focusing Surface-Acoustic-Wave Microcavities on GaAs

Madeleine E. Msall[1,2,*] and Paulo V. Santos[2,†]

[1] *Department of Physics and Astronomy, Bowdoin College, Brunswick, Maine 04011, USA*
[2] *Paul-Drude-Institut für Festkörperelektronik, Leibniz-Institut im Forschungsverbund e.V., 10117 Berlin, Germany*

(Received 15 August 2019; revised manuscript received 28 October 2019; published 22 January 2020)

Focusing microcavities for surface acoustic waves (SAWs) produce highly localized strain and piezoelectric fields that can dynamically control excitations in nanostructures. Focusing transducers (FIDTs) that generate SAW beams that match nanostructure dimensions require pattern correction due to diffraction and wave-velocity anisotropy. The anisotropy correction is normally implemented by adding a quadratic term to the dependence of the wave velocity on the propagation angle. We show that a SAW focusing to a diffraction-limited size in GaAs requires corrections that more closely follow the group-velocity wave front, which is not a quadratic function. Optical interferometric mapping of the resultant SAW displacement field reveals tightly focused SAW beams on GaAs with a minimal beam waist. An additional set of Gouy-phase–corrected passive fingers creates an acoustic microcavity in the focal region with a small volume and a high quality factor. Our $\lambda_{\mathrm{SAW}} = 5.6$ μm FIDTs are expected to scale well to the approximately 500-nm wavelength regime needed to study strong coupling between vibrations and electrons in electrostatic GaAs quantum dots.

DOI: 10.1103/PhysRevApplied.13.014037

I. INTRODUCTION

High-frequency surface acoustic waves (SAWs) can be effectively coupled to quantum registers such as point defects in diamond [1] and SiC [2], quantum dots [3–5], and transmon qubits [6,7]. Strong SAW coupling to quasi-zero-dimensional systems (e.g., quantum dots) requires the confinement of the acoustic field in high-quality-factor (Q) acoustic microcavities with dimensions comparable to the nanostructure sizes [8]. The latter can be achieved by generating the SAW using focusing interdigital transducers (FIDT) or by focusing the SAW field using acoustic lenses or horns [9,10].

A fundamental element in the design of FIDTs for tight focusing arises from the anisotropic propagation properties of SAWs on piezoelectric crystals. The fingers of FIDTs are curved to create a converging beam. Because the GaAs SAW phase velocity, v_{SAW}, changes with the wave-vector direction, the finger spacings of an FIDT must vary with angle in order to create a single resonance frequency across the device. The easiest way to visualize the required finger shape for a FIDT uses the time-reversal symmetry of the wave equation. A strain wave expanding from a point-excitation source will travel in real space carrying power as a group-velocity (v_g) wave front. By time reversal, a distributed source generating a focusing beam (corresponding to the FIDT finger shape) should mimic the profile of this group-velocity wave front.

Different approaches have been used to determine the shape of the GaAs v_g wave fronts. Optical images of fluid-surface deformation show the anisotropy in wave speed and the deviation of focus that occurs when anisotropy is not taken into account in finger design [11]. Imaging with stroboscopic synchrotron x-ray diffraction offers finer resolution and sensitivity to strain information [2,12]. SAW group-velocity maps are also produced in laser acoustic studies [13].

Previous work on FIDTs on GaAs has used quadratic approximations for the angular dependence of v_g and the phase velocity, v_{SAW} [14–16]. In this paper, we investigate the microscale strain field distribution of waves launched by FIDTs on GaAs (001) surfaces using scanning laser interferometry [17,18]. We show that although the quadratic approximation for v_g may be reasonable for FIDTs with very small angular apertures, it fails in FIDTs with wider angular apertures and small focusing waists. Significantly better focusing performances are obtained from FIDT designs that incorporate the full anisotropy of the elastic response and, thus, the real dependence of v_g on the propagation direction. Furthermore, we demonstrate that tighter energy confinement can be achieved

---

[*] mmsall@bowdoin.edu
[†] santos@pdi-berlin.de

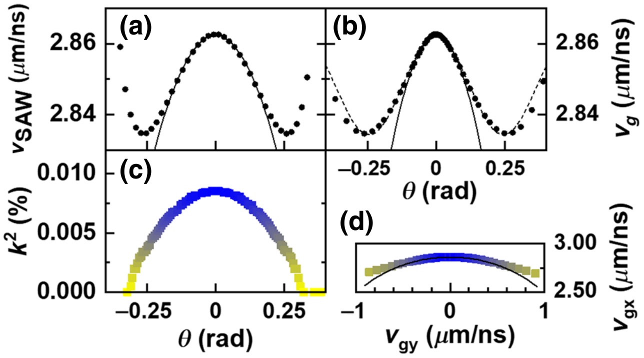

FIG. 1. The calculated (a) phase velocity, v_{SAW}, (b) group velocity, v_g, and (c) electromechanical coupling, k^2, as a function of the propagation angle θ with respect to a $\langle 110 \rangle$ direction of the GaAs (001) surface. (d) The group-velocity components $v_g = (v_{gx}, v_{gy})$ (colored squares). The FIDT fingers follow this curvature in real space. The color scale from (c) shows the strength of k^2 for the wave vectors that form each section of the wave front. The solid lines in (a), (b), and (d) show the quadratic approximations for the phase and group velocities from Ref. [16]. The dashed line in (b) is a fit with $v_g = 2848 + 13.7 \cos[4.1\pi\theta]$.

by combining FIDTs with acoustic microcavities and pattern correction for both material anisotropy [16] and beam diffraction [19]. Detailed views of the beam focusing show the complex interplay of acoustic anisotropy and wave diffraction in the formation of a tightly focused beam.

II. SURFACE WAVE FOCUSING IN GaAs

SAWs on GaAs (001) surfaces are normally excited along a piezoelectric $\langle 110 \rangle$ surface direction. Focusing requires the superposition of waves with a range of propagation angles, θ, with respect to the $\langle 110 \rangle$ surface direction. This range of angles is typically small ($|\theta| \lesssim 0.3$ rad), since the electromechanical coupling decreases with increasing θ, as shown in Fig. 1(c). In order to determine the group velocity, we numerically calculate the slope of the constant-frequency curve (i.e., the collection of k-space points with the same frequency) and find the surface normal, which indicates the real-space group-velocity direction. The difference between the group-velocity and k-vector directions is the beam steering angle. The group velocity in Fig. 1(b) is the phase speed divided by the cosine of this numerically determined beam steering angle. Figures 1(a) and 1(b) show the calculated phase and group velocities (symbols) as well as the corresponding quadratic approximations (solid lines) of de Lima *et al.* [16] The approximation noticeably deviates from the calculated group velocity after 0.1 rad and fails to model the velocity minima at $\theta = \pm 0.25$ rad. The dashed line in Fig. 1(b) shows a much better fit to the data using the cosine function listed in the figure caption.

The colored squares in Fig. 1(d) show the real-space curvature of the v_g wave front using Cartesian coordinates. This wave-front shape mirrors that of the FIDT fingers in our best focusing devices. A second FIDT design has finger shapes based on the quadratic approximation, shown as a solid line in Fig. 1(d). The finger shape calculated according to the group-velocity wave front is closer to a circular arc than the quadratic approximation. A wave-surface curvature that is a little larger than that of a circular arc, as we have here, is expected to be most effective for launching a narrow SAW beam [20]. The color scale in Fig. 1(d) illustrates that regions with the highest coupling on the finger pattern (blue squares with $k^2 \gtrsim 0.008\%$) are in a very narrow band of real-space angles near $\langle 110 \rangle$, where the wave-front curvature is quite flat.

The importance of having finger shapes precisely following the group-velocity wave fronts can be appreciated by considering that the substitution of the quadratic approximation of the wave speed, v_q, for the true v_g leads to a fractional phase shift

$$\frac{\Delta\phi}{\phi_{\mathrm{SAW}}} = \frac{v_g(\theta) - v_q(\theta)}{v_g(\theta)}. \tag{1}$$

As a result, errors in v_q as small as 0.5% lead to completely out-of-phase waveforms after propagation distances of roughly 50 λ_{SAW}. According to Fig. 1(b), v_q starts to deviate from v_g at angles $|\theta| \sim 0.1$ rad, for which k^2 is still more than 50% of its maximum value [cf. Fig. 1(c)]. Waves generated by fingers placed according to v_q will therefore destructively interfere at the focus even for very moderate angular apertures and numbers of FIDT fingers. The variation in piezoelectric coupling with the angle is expected to play a positive role in shaping the beam profile at the focus. The gradual decrease in strain generation at wide angles is preferable to a step function at the finger ends, creating a SAW beam profile that is more nearly Gaussian in cross section [19].

Using a scanning optical interferometer [Fig. 2(a)], we measure the effect of the finger shape on SAW focusing in FIDTs fabricated by electron-beam lithography [Fig. 2(b)]. The structures consist of two single-finger FIDTs (i.e., transducers with two fingers per SAW period with center-to-center distance $\lambda_{\mathrm{SAW}}/2$) with a length of 100 λ_{SAW} ($\lambda_{\mathrm{SAW}} = 5.6$ μm) and a full angular aperture $\theta_{\max} = 0.6$ rad. Due to acoustic Bragg reflections on the FIDT fingers, the 104 λ_{SAW} spacing between the FIDTs (corresponding to twice the focal length) forms a long microcavity (LC) confining the acoustic field. The finger metalization consists of a Ti/Al/Ti layer stack, with layer thicknesses of 10, 30, and 10 nm, respectively. The lower and upper Ti layers are included to improve adhesion to the substrate and reduce oxidation of the Al film, respectively.

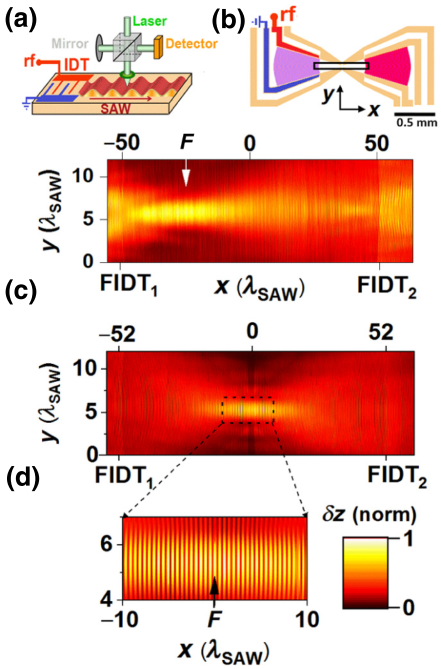

FIG. 2. (a) Interferometric detection of the SAW surface displacement, δz. (b) The long cavity (LC) defined by FIDTs. The rf drive is applied between the indicated electrodes of the left FIDT. The other electrodes (orange) are left floating. (c) The δz map for FIDTs with quadratic finger shapes (LC mode frequency $f_{\mathrm{SAW}} = 514$ MHz). The scan area [black box in (b)] is centered at $x = 0$ and overlaps the fingers at IDT$_1$ and IDT$_2$. (d) The δz map with group-velocity finger shapes (LC mode, $f_{\mathrm{SAW}} = 512.66$ MHz). The color scale represents the surface-displacement magnitude; the scan distance between neighboring maxima in the inset is $\lambda_{\mathrm{SAW}}/2$.

The negative impact of the quadratic approximation on the acoustic beam is clearly seen in Fig. 2(c). The rf-powered left FIDT concentrates the acoustic energy along the central line of the transducer (i.e., the x axis in Fig. 2) but the apparent focus is significantly displaced from the center of curvature (by 25 λ_{SAW}) to the point marked F. The displacement of the focus toward the transducer is consistent with the approximate wave front v_q shown in Fig. 1(d), which has a higher curvature than the v_g wave front [15]. In contrast, the FIDT in Fig. 2(d), with finger shapes that follow the v_g wave fronts, has a clear central focus. The inset shows nearly parallel wave fronts near the focal point and a minimum beam width of around λ_{SAW}.

III. SAW MICROCAVITIES

The relatively small angular aperture of the FIDTs in Fig. 2(b), which is limited by the reduction of the electromechanical coupling k^2 with θ, leads to a large longitudinal extension of the focused field of the LC. When addressing nanoscopic systems, however, the field concentration may be improved by inserting a second internal microcavity within the Rayleigh range of a LC (this combined structure will be denoted as "SC") [3,8]. Here, we exploit a key advantage of SAWs for manipulating or probing low-dimensional systems, namely that the acoustic excitation can be spatially separated from the interaction region with high field concentration.

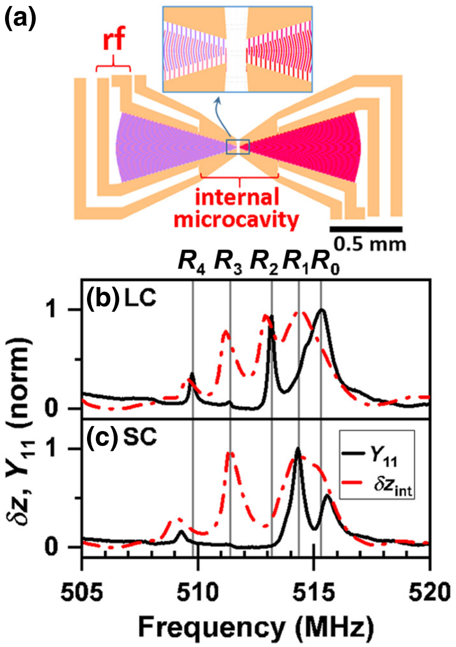

FIG. 3. (a) The short cavity (SC) defined by FIDTs and the finger pattern of the internal microcavity. The electrical and mechanical resonances for FIDTs in (b) the LC and (c) the SC cavity resonators are recorded by applying the rf power to the left FIDT, as indicated in (a). The other contacts are left floating. The principal modes of the long cavity (LC) are observed at $R_0 = 515.3$ MHz, $R_1 = 514.35$ MHz, $R_2 = 513.2$ MHz, $R_3 = 511.4$ MHz, and $R_4 = 509.8$ MHz. The admittance, Y_{11}, is derived from the scattering (S) rf parameters measured with a HP 8720D Network Analyzer. The integrated SAW displacement, δz_{int}, is the integrated interferometer signal along the FIDT axis near the focus.

In order to demonstrate the concept, we introduce in between the FIDTs the internal microcavity with a 4-λ_{SAW}-wide spacer shown in Fig. 3(a). The design includes separate contacts to the microcavity fingers that can be also directly excited with rf pulses. Alternatively, they can be connected to a dc bias when needed (e.g., for depletion of buried layers when gating quantum dots within the SC) or rf grounded to shield nanostructures within the SC from stray rf fields from the powered FIDT. These contacts are kept floating in the present field-mapping studies.

Since the internal microcavity is within the Rayleigh range of the FIDTs, an important design factor is the effect of diffraction on the wave focusing in the near field [14]. The impact of diffraction on the acoustic beam waist near the focus has been observed in water waves at the millimeter scale [21]. Correcting for diffraction requires changes in the curvature of the fingers as well as adjustments to the finger placement along the transducer axis. Without these corrections, the inner-transducer-finger contributions will be out of phase with those of the outer fingers, leading to destruction of the high-Q cavity.

For a focused two-dimensional (2D) Gaussian beam, the beam half-width, $\omega(x)$, corresponds to the transverse distance at which the amplitude reduces to $1/e$ and depends on the distance x to the focus:

$$\omega(x) = \omega_0\sqrt{1+\left(\frac{x}{x_R}\right)^2}, \tag{2}$$

where the Rayleigh length, x_R, defines the distance over which $\omega(x)$ increases by a factor of $\sqrt{2}$ from the minimum beam half-width, ω_0 [22]. The Rayleigh length is related to $\theta_{\max}$ and to ω_0 by

$$x_R = \frac{2\omega_0}{\theta_{\max}} = \frac{4\lambda_{\mathrm{SAW}}}{\pi\theta_{\max}^2}. \tag{3}$$

The net corrections for the FIDT fingers then include curvature corrections that depend upon the distance from the focus and the angle, θ, defining the off-axis position of a given finger element:

$$R(x_i,\theta) = x_i\left[1+\left(\frac{x_R}{x_i}\right)^2\right]R_{v_g}(\theta), \tag{4}$$

where x_i is the x coordinate of the ith finger and the factor $R_{v_g}(\theta) = v_g(\theta)/v_g(0)$ is the correction in the finger distance from the focal origin $x = 0$ due to the anisotropy of v_g.

A final phase correction to the position of the fingers is due to the Gouy phase, which results in an apparent increase of the acoustic wavelength as the beam moves through the focal point [23]. The Gouy phase correction for a 2D beam is

$$\Delta\phi_g(x) = \frac{1}{2}\arctan\left(\frac{x}{x_R}\right). \tag{5}$$

FIDT fingers are lithographically patterned with the shape determined by Eq. (4) at positions x_i that correspond to separations in total phase equal to π rad, including the Gouy-phase contribution. The thicknesses and widths of the fingers for the internal microcavity are the same as for the FIDTs.

In order to show the effects of the SC on the acoustic field distribution, the solid black curves in Figs. 3(b) and 3(c) compare the real parts of the electrical admittance, Y_{11}, of the FIDTs of the long [LC, cf. Fig. 2(b)] and short microcavities [SC, cf. Fig. 3(a)], respectively. The LC displays multiple peaks corresponding to different longitudinal modes. Here, the small shifts in the wavelength of the resonance enable the fitting of additional half-wavelengths between the emitting and reflecting FIDTs. With 104 λ_{SAW} between the two transducers, every additional half-wavelength results in a shift of approximately 2 MHz in the resonance frequency. Some of the modes have comparable Y_{11} amplitudes in both structures (e.g., modes R_0, R_1, and R_3). The amplitudes of the other modes are notably suppressed in the SC because they are not commensurate with the finger pattern of the internal microcavity.

The dotted-dashed red lines in Figs. 3(b) and 3(c) display the frequency dependence of the integrated SAW displacement δz_{int} near the focus measured by interferometry. For most of the modes, this amplitude compares well to the admittance resonances. The principal peak (R_1) near 514 MHz, for instance, is clearly visible in both the δz_{int} and Y_{11} curves. However, the displacement resonance at 511.4 MHz (R_3) is much stronger than the electrical resonance at the same frequency. The FIDT admittance, Y_{11}, relates the current through the device to the applied rf voltage: it is, therefore, proportional to the electric power coupled to the acoustic mode. The contrast between the very low admittance and the high surface displacement at R_3 indicates that this high-amplitude cavity oscillation is sustained at low input powers, as expected for a mode with a high Q. Measurement of the surface profile for R_3 with a denser frequency mesh (not shown) yields a Q of this cavity mode of 1900.

We now turn our attention to the strongly confined mode R_3. Images of the surface displacements of this mode in the LC and SC are compared in Figs. 4(a) and 4(b). Fits of scans along the y axis are used to extract the half-width [$\omega(x)$] and maximum surface displacement (δz_0) as a function of distance x from the focus displayed in Figs. 4(c) and 4(d), respectively. The dashed lines in these plots are obtained by fitting the measured data around the focus ($x = 0$) with Eq. (2) and with a Gaussian function, respectively, which yields the parameters summarized in Table I. Here, $2\sigma_x$ denotes the Gaussian mode length along x indicated in Figs. 4(c) and 4(d). Compared to the expected values for a Gaussian beam with a comparable 0.6-rad aperture, the R_3 modes for both cavities show comparable minimum beam half-widths but Rayleigh lengths that are almost twice as large. As seen in the inset of Fig. 2(d), the SAW displacement pattern in a LC is symmetric through the focus and shows nearly parallel wave fronts over an extension $\pm\Delta x_p \sim 10\ \lambda_{\mathrm{SAW}}$ around the focus, which is considerably longer than the Rayleigh $x_R = 3.5\ \lambda_{\mathrm{SAW}}$ determined from Eq. (3). For an acoustically isotropic material, the form of the Gaussian corrections in Eq. (4) predicts parallel wave fronts only within distances $\Delta x_p \lesssim x_R$ from the focus. The measured larger region

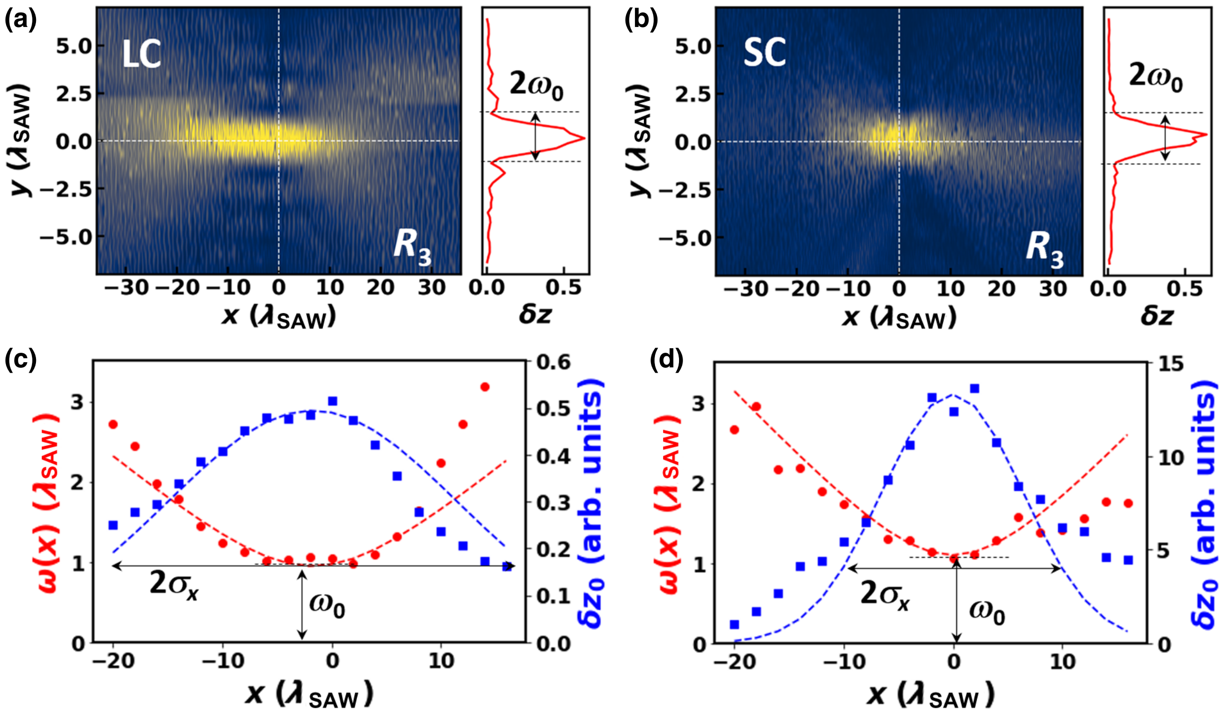

FIG. 4. Surface-displacement (δz) maps for the R_3 mode in (a) the long cavity (LC) and (b) the short cavity (SC). The right insets show profiles along the dashed horizontal lines indicated in the main plots. (c),(d) The dependence of the Gaussian-beam half-width ω (dots) and maximum displacement δz_0 (squares) on the position for mode R_3 in the LC and SC, respectively. The dashed red and blue lines are fits to Eq. (4) and to a Gaussian function, respectively, which yield the minimum beam half-width ω_0 and Gaussian width σ_x indicated in the figure.

(with $|\Delta x_p| \sim 3x_R$) must, therefore, be attributed to the acoustic anisotropy factor, $R_{v_g}(\theta)$. This anisotropic wavefront shape is directly related to the phonon focusing in this material, which concentrates the SAW energy along the $\langle 110 \rangle$ directions [24].

The profiles for δz_0 in Figs. 4(c) and 4(d) as well as the mode lengths in Table I show that R_3 is more spatially localized in the SC than in the LC. The mode area estimated according to $m_A = 4\sigma_x\omega_0 \ln 2$ for the SC (28 $\lambda_{SAW}{}^2$) is approximately 60% smaller than for the LC (49.3 $\lambda_{SAW}{}^2$), thus showing that the internal cavity can significantly enhance the acoustic confinement.

Finally, the SAW wave fronts should show the expected $\pi/2$ Gouy phase shift as the wave propagates within the Rayleigh range $|x| < x_R$ around the focus, as has been observed in femtosecond SAW pulses generated by ultrafast laser excitation [25]. The evolution of the Gouy phase, which is very important to the stabilization of the cavity mode, has so far not been directly measured for continuous SAW fields. In the present case, the prolonged Rayleigh length makes it challenging to detect the Gouy shifts. There are indeed some signs of appropriate phase shifts in the evolving beam in our data, but reproducible confirmation requires phase resolution just beyond what is achievable in our interferometric system.

TABLE I. Beam parameters for the R_3 mode.

Device	Half-width ω_0 (λ_{SAW})	Rayleigh length x_R (λ_{SAW})	Mode length $2\sigma_x$ (λ_{SAW})
Theory ($\theta_{max} = 0.6$)	1.06	3.54	
LC [Fig. 4(a)]	0.95 ± 0.04	8.2 ± 0.9	37.4 ± 2.0
SC [Fig. 4(b)]	1.1 ± 0.05	7.5 ± 1.0	18.4 ± 1

IV. CONCLUSION

We demonstrate diffraction-limited focusing and tight confinement of surface acoustic beams using acoustic microcavities defined by FIDTs on GaAs. GaAs-based nanodevices are the basis for a wide range of compact circuits for the implementation of quantum functionalities [26]. Our FIDT designs, which are also applicable to other acoustically anisotropic materials, offer opportunities for measurement and control of low-dimensional systems by highly confined strain fields. In FIDT design, it is important to understand the unexpected sensitivity of the beam profiles to small changes, especially for short-wavelength and high-frequency applications. As the operating frequency increases, dispersion effects arising from the finite thickness of the FIDT fingers may require further refinements of the FIDT shape. In fact, we have also carried out finite-element simulations [8] for focusing microcavities for an acoustic wavelength of 500 nm (corresponding to a resonance frequency around 5 GHz), which show that the design scales well to submicrometer acoustic wavelengths.

ACKNOWLEDGMENTS

We thank Stefan Ludwig and Jonas Lähneman for discussions and comments on the manuscript, as well as Sebastian Meister for the expertise in device fabrication. M.E.M. and P.V.S. acknowledge financial support from the German Academic Exchange Service (Deutscher Akademischer Austauschdienst, DAAD) (Grant No. 57314018) and the Deutsche Forschungsgemeinschaft (DFG) (Grant No. 4056192179), respectively.

---

[1] D. A. Golter, T. Oo, M. Amezcua, K. A. Stewart, and H. Wang, Optomechanical Quantum Control of a Nitrogen-Vacancy Center in Diamond, Phys. Rev. Lett. **116**, 143602 (2016).

[2] S. J. Whiteley, G. Wolfowicz, C. P. Anderson, A. Bourassa, H. Ma, M. Ye, G. Koolstra, K. J. Satzinger, M. V. Holt, F. J. Heremans, A. N. Cleland, D. I. Schuster, G. Galli, and D. D. Awschalom, Spin-phonon interactions in silicon carbide addressed by Gaussian acoustics, Nat. Phys. **15**, 490 (2019).

[3] J. C. H. Chen, Y. Sato, R. Kosaka, M. Hashisaka, K. Muraki, and T. Fujisawa, Enhanced electron-phonon coupling for a semiconductor charge qubit in a surface phonon cavity, Sci. Rep. **5**, 15176 (2015).

[4] M. Metcalfe, S. M. Carr, A. Muller, G. S. Solomon, and J. Lawall, Resolved Sideband Emission of InAs/GaAs Quantum Dots Strained by Surface Acoustic Waves, Phys. Rev. Lett. **105**, 037401 (2010).

[5] S. Lazic, A. Hernández-Mínguez, and P. V. Santos, Control of single photon emitters in semiconductor nanowires by surface acoustic waves, Semicond. Sci. Technol. **32**, 084002 (2017).

[6] M. Gustafsson, P. V. Santos, G. Johansson, and P. Delsing, Local probing of propagating acoustic waves in a gigahertz echo chamber, Nat. Phys. **8**, 338 (2012).

[7] B. A. Moores, L. R. Sletten, J. J. Viennot, and K. W. Lehnert, Cavity Quantum Acoustic Device in the Multimode Strong Coupling Regime, Phys. Rev. Lett. **120**, 227701 (2018).

[8] P. V. Santos, M. Msall, and S. Ludwig, in *2018 IEEE Ultrasonics Symposium* (IEEE, New York, 2018).

[9] R. M. White, in *Proc. of the IEEE* (IEEE, New York, 1970), Vol. 58, p. 1238.

[10] I. Yao, in *Proc. of the 1980 IEEE Ultrasonics Symposium*, edited by B. R. McAvoy (IEEE, New York, 1980), p. 37.

[11] R. W. Rambach, J. Taiber, C. M. L. Scheck, C. Meyer, J. Reboud, J. M. Cooper, and T. Franke, Visualization of surface acoustic waves in thin liquid films, Sci. Rep. **6**, 21980 (2016).

[12] W. Sauer, M. Streibl, H. T. Metzger, A. G. C. Haubrich, S. Manus, A. Wixforth, J. Peisl, A. Mazuelas, J. Härtwig, and J. Baruchel, X-ray imaging and diffraction from surface phonons on GaAs, Appl. Phys. Lett. **75**, 1709 (1999).

[13] A. A. Maznev, A. M. Lomonosov, P. Hess, and A. A. Kolomenskii, Anisotropic effects in surface acoustic wave propagationfrom a point source in a crystal, Eur. Phys. J. **B35**, 429 (2003).

[14] I. M. Mason and E. A. Ash, Acoustic surface wave beam diffraction on anisotropic substrates, J. Appl. Phys. **42**, 5343 (1971).

[15] J. B. Green, G. S. Kino, and B. T. Khuri-Yakub, in *Proceedings of the 1980 IEEE Ultrasonics Symposium*, edited by B. R. McAvoy (IEEE, New York, 1980), p. 69.

[16] M. M. de Lima, Jr., F. Alsina, W. Seidel, and P. V. Santos, Focusing of surface-acoustic-wave fields on (100) GaAs surfaces, J. Appl. Phys. **94**, 7848 (2003).

[17] M. M. de Lima, Jr. and P. V. Santos, Modulation of photonic structures by surface acoustic waves, Rep. Prog. Phys. **68**, 1639 (2005).

[18] J. V. Knuuttila, P. T. Tikka, and M. M. Salomaa, Scanning Michelson interferometer for imaging surface acoustic wave fields, Opt. Lett. **25**, 613 (2000).

[19] G. S. Kino, *Acoustic Waves: Devices, Imaging and Analog Signal Processing* (Prentice-Hall, Englewood Cliffs, N.J, 1987).

[20] T.-T. Wu, H.-T. Tang, Y.-Y. Chen, and P.-L. Liu, Analysis and design of focused interdigital transducers, IEEE Trans. Ultrason. Ferroelectr. Freq. Control **52**, 1384 (2005).

[21] R. Longo, S. Vanlanduit, G. Arroud, and P. Guillaume, Underwater acoustic wavefront visualization by scanning laser doppler vibrometer for the characterization of focused ultrasonic transducers, Sensors **15**, 19925 (2015).

[22] J. Alda, *Encyclopedia of optical engineering* (Taylor & Francis Inc, Bosa Roca, USA, 2003), Chap. Laser and Gaussian beam propagation and transformation, p. 999.

[23] S. Feng and H. G. Winful, Physical origin of the Gouy phase shift, Opt. Lett. **26**, 485 (2001).

[24] J. P. Wolfe, *Imaging Phonons: Acoustic Wave Propagation in Solids* (Cambridge University Press, Cambridge, 1998).

[25] A. A. Kolomenskii, S. N. Jerebtsov, and H. A. Schuessler, Focal transformation and the Gouy phase shift of converging one-cycle surface acoustic waves excited by femtosecond laser pulses, Opt. Lett. **30**, 2019 (2005).

[26] C. P. Dietrich, A. Fiore, M. G. Thompson, M. Kamp, and S. Höfling, GaAs integrated quantum photonics: Towards compact and multi-functional quantum photonic integrated circuits, Laser Photon. Rev. **10**, 870 (2016).